

# Antiferromagnetic spin valve of graphene heterostructure

Ma Luo\*

*The State Key Laboratory of Optoelectronic Materials and Technologies  
School of Physics  
Sun Yat-Sen University, Guangzhou, 510275, P.R. China*

Spin valves consisted of heterostructures of single-layer graphene on antiferromagnetic substrate, or bilayer graphene intercalated between two (anti)ferromagnetic insulators, are proposed. The magnetization orientation of the antiferromagnetic substrate(s) control the band gap and topological properties, and then control the charge, spin and(or) valley conductivities. The heterostructures are investigated by tight binding model with the exchange field induced by the Van der Waals interaction between the graphene and the (anti)ferromagnetic substrate(s), the Hubbard model that describe the electron-electron interaction and the spin orbital coupling. Novel effect of the Hubbard interaction to the band gap are found to strengthen or weaken the spin valve efficiency. Topological edge states at the domain walls between regions with different Chern numbers are confirmed by the tight binding calculation of nanoribbons. The presence of the Hubbard model induces the quantum anomalous Hall phase in some heterostructures which is topologically trivial in the absence of interaction.

PACS numbers: 00.00.00, 00.00.00, 00.00.00, 00.00.00

## I. INTRODUCTION

Spintronic has been proposed as physical foundation of information processing system. The phenomenon of spin-dependent transport based on the physics of giant magnetoresistance [1, 2] and tunnel magnetoresistance [3, 4] have been studied and further developed into the widely applied information storage devices known as Magnetoresistive random-access memory (MRAM). The concept of spin valve [5] that controls the electronic conductivity by the magnetization orientation lead to development of spintronic for information operating systems, in addition to information storage medium.

Graphene have been considered as preeminent candidates for spintronic systems [6–8], because of the high electron mobility [9, 10] and long spin relaxation life time [11–14]. Generation and manipulation of spin current by electronic [15, 16] and optical [17–22] method have been proposed theoretically and studied experimentally [23–25]. Single layer graphenes (SLGs) and bilayer graphenes (BLGs) with substrate proximity effect [26–28] or adatom doping [29] exhibit large spin orbital coupling (SOC) that make the spintronic effect observable in room temperature. Specifically, the graphene on transition metal dichalcogenides (TMDCs) systems are found to induce novel spin effect and topological properties [30–35]. Proximity effect of graphene on ferromagnetic insulator induces exchange field, which is spin dependent potential [36]. Coexistence of ferromagnetic exchange field and Rashba SOC drive the SLGs into quantum anomalous Hall (QAH) phase [37, 38]. The topological zero-line mode at the domain wall of QAH phase host topological edge states with localized one-way charge transportation [39]. Van der Waals spin valves based on BLGs het-

erostructures [40] have been recently proposed [41].

In order to reduce power consumption and device size of the spintronic systems, antiferromagnetic materials have been proposed to replaced the ferromagnets [42, 43]. Comparing to ferromagnetic spintronic, the spintronic devices based on antiferromagnetic materials have multiple advantages, such as absence of parasitic stray fields and ultrafast magnetization dynamics. The antiferromagnetic insulators with high Neel temperature have been studied experimentally [44–47], including materials with hexagonal crystal structure [44, 45].

In order to harness the advantages of both graphene and antiferromagnetic spintronic, we propose spin valve based on heterostructures of graphene and antiferromagnetic materials. Assuming that the antiferromagnetic insulator with surface lattice being matched to graphene could be found or engineered, the staggered sublattice exchange field are induced in the graphene. We consider SLGs on the antiferromagnetic substrate, BLGs being intercalated between two antiferromagnetic substrates and BLGs being intercalated between an antiferromagnetic substrate and a ferromagnetic substrate. Additional proximity to TMDCs or adatom doping induce SOC that modify the topological properties. For bulk graphene, the band gap and conductivity are controlled by flipping the magnetization orientation of the antiferromagnetic substrates. In addition to charge conductivity, valley or spin polarized conductivities are also controlled by the magnetization and SOC. For one groups of the intercalated BLGs, the Rashba SOC induce the QAH phase in the absence of the Hubbard interaction. For the other groups of the intercalated BLGs, in the absence of the Hubbard interaction, the systems is topological trivial for arbitrary Rashba SOC; the presence of the Hubbard interaction drives the systems into the QAH phase [48, 49]. For the (anti)ferromagnetic domain wall, the topological edge states with conductivity being controlled by the magnetization orientation are also

---

\*Corresponding author: luom28@mail.sysu.edu.cn

investigated.

The article is organized as following: In section II, the tight binding model for SLG is given, and the calculation method of the topological number are briefly discussed. The first subsection discusses the effect of the Hubbard interaction to the band structure and bulk band gap. The second subsection discusses the topological phase in the presence of the Rashba and intrinsic SOC. In section III, the tight binding modeling for the BLG are given. The first subsection discusses the effect of the Hubbard interaction to the band structure and bulk band gap. The second subsection describes the condition to induce quantum anomalous Hall phase and the topological edge states at the domain wall between regions with different Chern numbers. The third subsection discussed the combination effect of Rashba SOC and Hubbard interaction on the topological properties. In section IV, the conclusion is given.

## II. SINGLE-LAYER GRAPHENE

The pristine SLG is described by the tight binding Hamiltonian

$$H_0 = - \sum_{\langle i,j \rangle, \sigma} t c_{i\sigma}^+ c_{j\sigma} \quad (1)$$

where  $t = 2.8$  eV is the hopping energy,  $\sigma = \pm 1$  is the index of spin,  $i$  and  $j$  are the indices of lattice sites,  $c_{i\sigma}^+$  ( $c_{i\sigma}$ ) is the creation(annihilation) operator of electron at the  $i$ -th lattice site with spin index  $\sigma$ . The summation indices with  $\langle i, j \rangle$  cover the nearest neighboring lattice sites. Assuming that the SLG is proximitized to the lattice matching antiferromagnetic insulator, the spin-dependent staggered sublattice exchange field is modelled by the Hamiltonian as

$$H_{AF}^{x,y,z} = \lambda_{AF}^{x,y,z} \sum_{i,\sigma,\sigma'} \kappa_i \hat{s}_{\sigma,\sigma'}^{x,y,z} c_{i\sigma}^+ c_{i\sigma'} \quad (2)$$

where  $\hat{s}^{x,y,z}$  are the Pauli matrix of spin x, y and z. In this manuscript,  $\kappa_i$  is equal to 1(-1) for the A(B) sublattice. On the other hand, the spin-independent staggered sublattice potential induced by the nonmagnetic substrate, such as h-BN or SiC, is modelled by the Hamiltonian

$$H_{\Delta} = \lambda_{\Delta} \sum_{i,\sigma} \kappa_i c_{i\sigma}^+ c_{i\sigma} \quad (3)$$

In case that the proximity substrate is ferromagnetic insulator, the exchange field is ferromagnetic like, which is given as [50]

$$H_{FM}^{x,y,z} = \lambda_{FM}^{x,y,z} \sum_{i,\sigma,\sigma'} \hat{s}_{\sigma,\sigma'}^{x,y,z} c_{i\sigma}^+ c_{i\sigma'} \quad (4)$$

If the other surface of the SLG is proximitized to TMDCs, or covered by appropriate adatom doping, Rashba and

intrinsic SOC are induced. The Rashba SOC is described by the Hamiltonian

$$H_R = \frac{2i\lambda_R}{3} \sum_{\langle i,j \rangle, \sigma, \sigma'} [(\hat{\mathbf{s}} \times \mathbf{d}_{ij})_z]_{\sigma, \sigma'} c_{i\sigma}^+ c_{j\sigma'} \quad (5)$$

where  $\mathbf{d}_{ij}$  is the unit vector from the  $i$ -th to  $j$ -th lattice site,  $\hat{\mathbf{s}}$  is the vector of three Pauli matrix for spin. The proximity effect of the TMDCs induce staggered sublattice intrinsic SOC given by [30, 31, 34]

$$H_{sI} = \frac{i\lambda_{sI}}{3\sqrt{3}} \sum_{\langle\langle i,j \rangle\rangle, \sigma, \sigma'} \kappa_i \nu_{ij} \hat{s}_{\sigma, \sigma'}^z c_{i\sigma}^+ c_{j\sigma'} \quad (6)$$

where  $\nu_{ij} = (+1) - 1$  for (counter)clockwise path. The summation indices with  $\langle\langle i, j \rangle\rangle$  cover the next-nearest neighboring lattice sites. The regular intrinsic SOC induced by other systems is given by

$$H_I = \frac{i\lambda_I}{3\sqrt{3}} \sum_{\langle\langle i,j \rangle\rangle, \sigma, \sigma'} \nu_{ij} \hat{s}_{\sigma, \sigma'}^z c_{i\sigma}^+ c_{j\sigma'} \quad (7)$$

In the presence of interaction that is described by the Hubbard model, the additional Hamiltonian is

$$H_U = U \sum_i n_{i\sigma} n_{i\bar{\sigma}} \quad (8)$$

where  $n_{i\sigma}$  is the operator of the particle number at the  $i$ -th lattice with spin indices  $\sigma$  and  $\bar{\sigma} = -\sigma$ . In the presence of  $H_U$ , the spectral functions of the bulk and nanoribbon systems are calculated by applying the cluster perturbation theory(CPT) method [51–56].

The topological properties of the systems can be described by the Chern number and valley Chern number. The topological numbers are calculated for non-interacting systems. The Chern number being denoted as  $\mathcal{C}$  is defined as the integral of the Berry curvature of the occupied bands of an insulator covering the whole first Brillouin zone [37, 38]. Because the Berry curvature have large value in the vicinity of K(K') point, the Chern number of each valley being denoted as  $\mathcal{C}_{K(K')}$  can be defined for the corresponding continuum Dirac Fermion model [57, 58]. In this case, the integral of the Berry curvature of the continuum Dirac Fermion model cover the infinite large Brillouin zone. The difference between the Chern number of K and K' valley is the valley Chern number  $\mathcal{C}_V = \mathcal{C}_K - \mathcal{C}_{K'}$ . For the system without spin flipping term in the Hamiltonian, the Chern number of each spin component and each valley can be defined for the corresponding continuum Dirac Fermion model as well, which is denoted as  $\mathcal{C}_{K(K')}^\sigma$ . Similarly, the valley Chern number of each spin component can be defined as  $\mathcal{C}_V^\sigma = \mathcal{C}_K^\sigma - \mathcal{C}_{K'}^\sigma$ .

In the sole presence of antiferromagnetic exchange field or staggered sublattice potential, which are described by the Hamiltonian  $H_0 + H_{\Delta}$  or  $H_0 + H_{AF}^z$ , the spin flipping term is absent. Both of these two Hamiltonian describe massive Dirac Fermion. The former model has the

same mass term for each spin component, while the later model has mass terms with opposite sign for the two spin components. Since the band gaps only depend on the absolute value of the mass terms, the two models have the same band structure, assuming  $\lambda_\Delta = \lambda_{AF}^z$ . If the magnetization orientation is parallel to the graphene plane, such as  $H_0 + H_{AF}^x$ , the band structure remains the same. For the model  $H_0 + H_{AF}^z$ , the spin and valley dependent Chern number is  $C_\tau^\sigma = \tau\sigma$  with  $\tau = \pm 1$  labeling the K(K') valley. Similar to the domain wall between two regions with staggered sublattice potential of opposite sign [59, 60], the domain wall between two regions with antiferromagnetic exchange fields of opposite magnetization orientations support chiral edge states. The dispersions of the chiral edge states of the opposite spin components are opposite to each other in each valley. As a result, the chiral edge states support dissipationless spin-valley current at the intrinsic Fermi level [61].

### A. Bulk band gap: effect of Hubbard interaction

In this subsection, we study the effect of the Hubbard interaction to the bulk band gap and compare the two models with the Hamiltonian  $H_0 + H_\Delta$  and  $H_0 + H_{AF}^z$ . In the absence of the Hubbard interaction, assuming the parameters  $\lambda_\Delta = \lambda_{AF}^z = 28$  meV, the band structures of the two Hamiltonian are the same, as shown in Fig. 1(a) and (b). The effect of the interaction is described by adding  $H_U$  to each model. The spectral function given by the CPT method are plotted as shaded surface in Fig. 1(a) and (b). In the presence of interaction, with the realistic parameter  $U = 1.6t$ , the spectral function of these two systems exhibit different feature. For the Hamiltonian  $H_0 + H_\Delta + H_U$ , the gap of the Dirac Fermion is suppressed to near zero, as shown in Fig. 1(a). Similar conclusion was given by the theoretical calculation of the Hubbard model by applying dynamical mean field theory [62, 63]. In addition, the interaction shifts the center of the valleys [56]. In contrary, for the Hamiltonian  $H_0 + H_{AF}^z + H_U$ , the gap is enlarged by the interaction, as shown in Fig. 1(b). The phenomenon can be understood by the picture of mean field approximation that the Hubbard model is approximated as  $H_U \approx U \sum_i (n_{i+} \langle n_{i-} \rangle + n_{i-} \langle n_{i+} \rangle)$ . The  $\langle n_{i\sigma} \rangle$  at A sublattice is larger(smaller) than that at B sublattice, if the local potential of the opposite spin at A sublattice is smaller(larger) than that at B sublattice. The mean field Hubbard terms act as another mass term of the Dirac Fermion. For the systems with  $H_0 + H_\Delta + H_U$ , the effective mass term of the Hubbard model partially cancel the mass term of the staggered sublattice potential. In contrary, for the systems with  $H_0 + H_{AF}^z + H_U$ , the effective mass term of the Hubbard model has the same sign as the mass term of the staggered sublattice potential, so that the gap is enlarged. Further consideration of the short range correlation by the CPT method modifies the band gap and shift the center of the valleys. In case that the

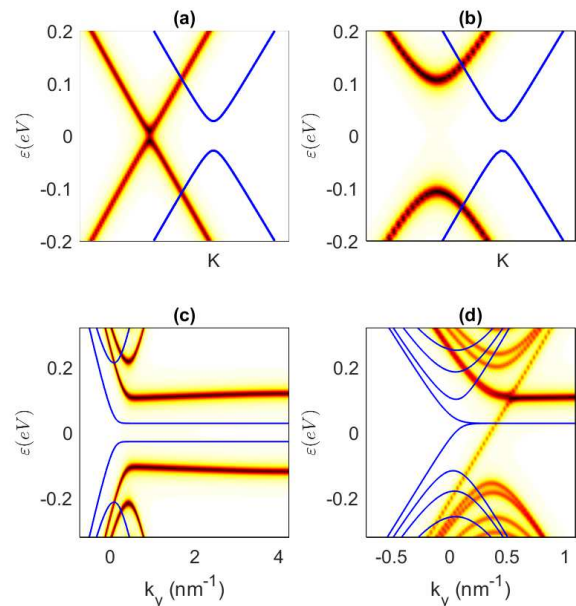


FIG. 1: The shaded surface and blue solid lines are the spectral function and band structure in the  $\epsilon - k$  space, respectively. (a) is for the graphene with staggered sublattice potential modelled by the Hamiltonian  $H_0 + H_\Delta + H_U$ . (b), (c) and (d) are for the graphene with antiferromagnetic exchange field modelled by the Hamiltonian  $H_0 + H_{AF}^z + H_U$ . (a) and (b) are for the bulk systems. (c) and (d) are for the zigzag nanoribbon with 60 and 120 unit cells, respective. In (d), the magnetization orientations of the left and right halves of the nanoribbon are opposite to each other. Only the band structure and spectral function of the spin up component are plotted in (d).

orientation of the magnetization of the antiferromagnetic substrate is parallel to the graphene plane, for example, only  $H_{AF}^x$  and(or)  $H_{AF}^y$  present, the band structure and the spectral function maintain the same features as those of the Hamiltonian  $H_0 + H_{AF}^z + H_U$ .

Because of the opening of the bulk band gap, the zigzag nanoribbon also exhibit band gap, as shown in Fig. 1(c). The localized flat band become slightly bended with small dispersion in the presence of the Hubbard interaction. In order to design localized spin valve with small scale, the spin dependent chiral edge states at the domain wall between two regions with opposite magnetization orientations of the antiferromagnetic substrates are investigated. In the absence of the Hubbard interaction, the chiral edge states of the domain wall between two semi-infinite graphene have dispersion relation  $\epsilon = \sigma\tau\hbar v_F k_y$  near to the K(K') valley, with  $k_y$  being the wave number along the domain wall. Because of the finite size effect, the chiral edge state at the domain wall couple with the edge states at the zigzag open boundaries, so that the dispersion deviate from linear, as shown by the blue(solid) line in Fig. 1(d). The presence of the Hubbard interaction enlarge the bulk band gap as well as weaken the finite size effect. Thus, the dispersion of the chiral edge

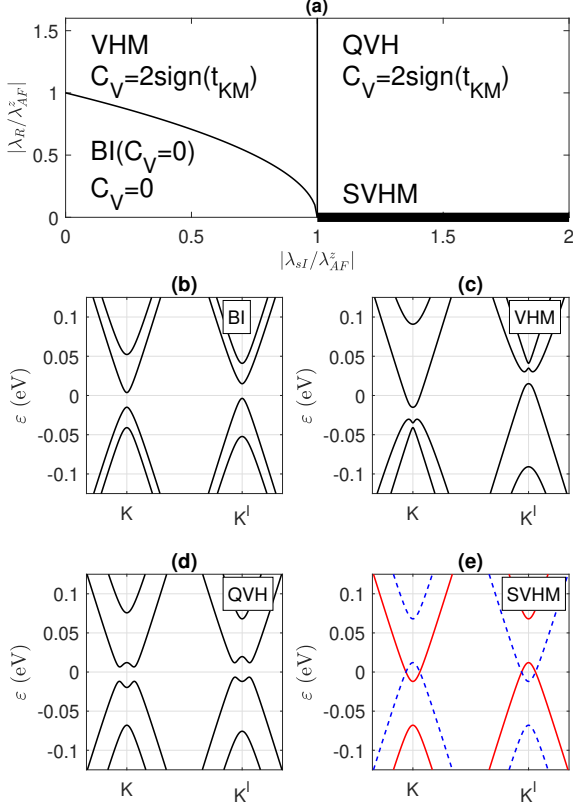


FIG. 2: (a) The phase diagram in the  $\lambda_R - \lambda_{sI}$  space with nonzero  $\lambda_{AF}^z$  of the model with the Hamiltonian  $H_0 + H_{AF}^z + H_R + H_{sI}$ . The band structures of BI, VHM, QVH and SVHM phases are plotted in (b), (c), (d) and (e), respectively. In (e), the band structures of the spin up and down components are plotted as red(solid) and blue(dash) lines, respectively.

states remain linear in a larger bandwidth, as shown by the spectral function in Fig. 1(d).

## B. Topological phase diagram

In the presence of the SOC, the SLGs are described by the Hamiltonian  $H_0 + H_{AF}^z + H_R + H_{(s)I}$ . For the realistic materials being proximitized to TMDCs,  $H_\Delta$  appears and the intrinsic SOC includes both  $H_{sI}$  and  $H_I$ . In order to demonstrate the physics qualitatively, we neglect  $H_\Delta$  and separately consider the sole presence of  $H_{sI}$  or  $H_I$ . In the absence of  $H_{AF}^z$ , the model with  $H_0 + H_R + H_{sI}$  is in the quantum valley Hall(QVH) phase with  $\mathcal{C} = 0$  and  $\mathcal{C}_V = 2 \cdot \text{sign}(\lambda_{sI})$ . On the other hand, the model with  $H_0 + H_R + H_I$  is in the trivial band insulator(BI) phase with  $\mathcal{C} = 0$  and  $\mathcal{C}_V = 0$ .

In the presence of  $H_{AF}^z$ , the phase diagram of the model with the Hamiltonian  $H_0 + H_{AF}^z + H_R + H_{sI}$

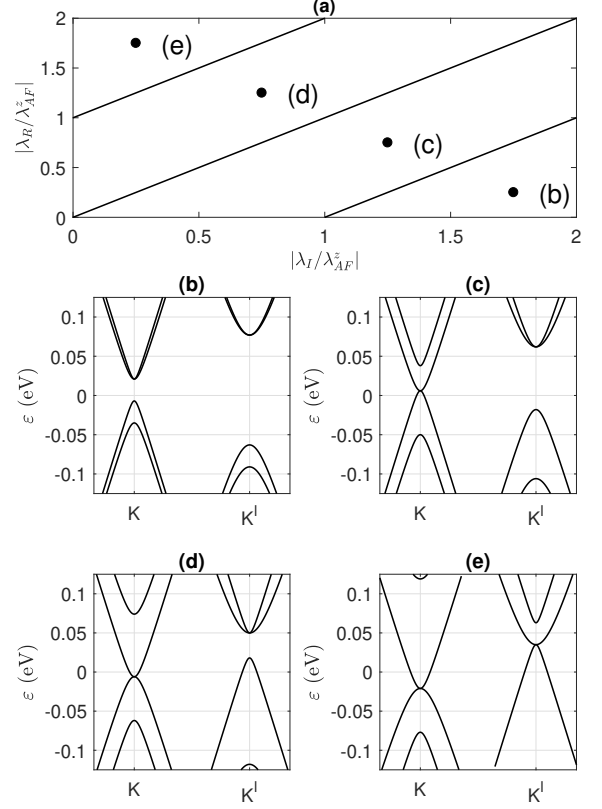


FIG. 3: (a) The phase diagram in the  $\lambda_R - \lambda_I$  space with nonzero  $\lambda_{AF}^z$  of the model with the Hamiltonian  $H_0 + H_{AF}^z + H_R + H_I$ . The band structures of the phases marked by the black dots in each phase regime are plotted in (b) to (e).

are plotted in Fig. 2(a). In the regime with  $\lambda_{sI} < \lambda_{AF}^z$ , two phases appear, which are BI and valley half-metal(VHM). The band structure of the systems in BI and VHM phases are plotted in Fig. 2(b) and (c), respectively. By solving the Hamiltonian at K(K') point, the condition of gap closing is given as  $\lambda_R = \sqrt{\lambda_{AF}^z(\lambda_{AF}^z - \lambda_{sI})}$ , which is the phase boundary between BI and VHM. Assuming full occupation of the valence band, the VHM phase has the same topological number as the QVH phase. However, the global gap of the VHM phase is closed, because the gaps of K and K' valley does not align. In equilibrium, the conduction(valence) band of the K(K') valley is partially occupied(empty). The conductance of K(K') valley is electron(hole) like, so that this phase is name as valley half-metal. By tuning the Fermi level into the gap of K(K') valley, the conductance is K'(K) valley polarized. Increasing  $\lambda_{sI}$  across the vertical line  $\lambda_{sI} = \lambda_{AF}^z$  in the phase diagram bring the systems back to the QVH phase with global gap. The band structure of the QVH phase is plotted in Fig. 2(d). When  $\lambda_R$  equate zero in this regime(thick line in the phase di-

agram), the band structure is plotted in Fig. 2(e), which is gapless. For each spin component, the conduction is valley half-metal like, and the valley polarization for the two spin component is opposite, so that this phase is denoted as the spin-valley half-metal(SVHM). If the absolute value of the Fermi level is tuned to be larger than  $\lambda_{sI} - \lambda_{AF}^z$ , the systems exhibit coupled spin and valley physics [64].

On the other hand, the phase diagram of the model with the Hamiltonian  $H_0 + H_{AF}^z + H_R + H_I$  is simpler since all phases are topological trivial, as shown in Fig. 3(a). The model with the Hamiltonian  $H_0 + H_R + H_I$  is in quantum spin Hall phase with topological number  $Z_2 = 1$  [65], but the presence of the antiferromagnetic exchange field break the time-reversal symmetry and drive the system into topological trivial phase. The band structures of four phases marked by the black dot and the corresponding title in Fig. 3(a) are plotted in Fig. 3(b-e). The three straight lines that separate the four phases are  $\lambda_R = \lambda_I - \lambda_{AF}^z$ ,  $\lambda_R = \lambda_I$  and  $\lambda_R = \lambda_I + \lambda_{AF}^z$ . The phase in regime (b) is band insulator. The phase in regime (c) is valley polarized semi-metal(VPSM), because the band gap of only one valley is closed, and the intrinsic Fermi level is within the gap of the other valley. For the phase in regime (d), the gap of K' valley remains open. The Dirac point of K valley drop bellow the top of valence band of the K' valley, so that the intrinsic Fermi level cross the conduction(valence) band of K(K') valley. For the phase in regime (e), the gap of K' valley is closed.

### III. BILAYER GRAPHENE

The Hamiltonian of each graphene layer are given by Eq. (1-8) with an additional layer index  $\nu$ , i.e.  $H_{0,\nu}$ ,  $H_{\Delta,\nu}$ ,  $H_{AF,\nu}^{x,y,z}$ ,  $H_{FM,\nu}^{x,y,z}$ ,  $H_{R,\nu}$ ,  $H_{(s)I,\nu}$  and  $H_{U,\nu}$ . The index  $\nu = 1$  or  $\nu = 2$  labels the top or bottom graphene layer, respectively. The hopping between two graphene layers is described by the Hamiltonian

$$H_{\perp} = t_{\perp} \sum_{\langle i,j \rangle_{\perp}, \sigma} c_{i\sigma}^{\dagger} c_{j\sigma} \quad (9)$$

where the summation indices  $\langle i,j \rangle_{\perp}$  couple the B lattice sites of the  $\nu = 1$  layer and the nearest A lattice site of the  $\nu = 2$  layer. The spin valve consisted of BLGs being intercalated between two ferromagnetic insulators, which are modelled by the Hamiltonian  $\sum_{\nu} (H_{0,\nu} + H_{FM,\nu}^z) + H_{\perp}$  were investigated in Ref. [41]. The BLGs with  $\lambda_{FM,1}^z = \lambda_{FM,2}^z$  are conductor, and the BLGs with  $\lambda_{FM,1}^z = -\lambda_{FM,2}^z$  are insulator. We investigated the BLGs being intercalated between two antiferromagnetic insulators, being modelled by the Hamiltonian  $\sum_{\nu} (H_{0,\nu} + H_{AF,\nu}^{(x)}) + H_{\perp}$ , and the BLGs being encapsulated between antiferromagnetic insulator and ferromagnetic insulator, being modelled by the Hamiltonian  $\sum_{\nu} H_{0,\nu} + H_{AF,\nu}^{(x)} + H_{FM,\bar{\nu}}^z + H_{\perp}$  with  $\bar{\nu} = 3 - \nu$ . The BLGs being intercalated between two nonmagnetic substrate are modelled by the Hamiltonian  $\sum_{\nu} (H_{0,\nu} + H_{\Delta,\nu}) + H_{\perp}$ .

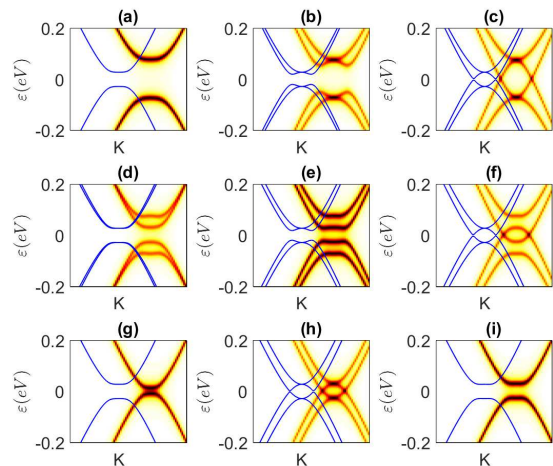


FIG. 4: The band structure and spectral function of the BLGs being intercalated between two antiferromagnetic insulators with the nonzero coefficients being  $\lambda_{AF,1}^z = \lambda_{AF,2}^z = 28$  eV in (a),  $\lambda_{AF,1}^z = \lambda_{AF,2}^x = 28$  eV in (b) and  $\lambda_{AF,1}^z = -\lambda_{AF,2}^z = 28$  eV in (c). Those of the BLGs being intercalated between ferromagnetic insulator at the top and antiferromagnetic insulator at the bottom with the nonzero coefficients being  $\lambda_{FM,1}^z = \lambda_{AF,2}^z = 28$  eV in (d),  $\lambda_{FM,1}^z = \lambda_{AF,2}^x = 28$  eV in (e) and  $\lambda_{FM,1}^z = -\lambda_{AF,2}^z = 28$  eV in (f). Those of the BLGs being intercalated between nonmagnetic substrates with  $\lambda_{\Delta,1} = \lambda_{\Delta,2} = 28$  eV in (g). Those of the BLGs being intercalated between two ferromagnetic insulators with the nonzero coefficients being  $\lambda_{FM,1}^z = \lambda_{FM,2}^z = 28$  eV in (h) and  $\lambda_{FM,1}^z = -\lambda_{FM,2}^z = 28$  eV in (i).

#### A. Bulk band gap

The band structures and spectral functions of the BLGs being intercalated between two antiferromagnetic insulators are plotted in Fig. 4(a-c). In Fig. 4(a), when the magnetization orientations of the top and bottom layer are the same, the band structure has a gap. The Hubbard interaction enlarge the band gap, being similar to the situation in SLGs. When the magnetization orientation of the bottom layer is rotated to be perpendicular to that of the top layer, the degenerated band split up, and the band gap slightly decreases, as shown in Fig. 4(b). Further rotating the magnetization orientation of the bottom layer to be opposite to that of the top layer closes the gap, as shown in Fig. 4(c). The BLGs were switched from insulator to conductor by rotating the magnetization orientation of the top or bottom antiferromagnetic substrate. This property could be used to construct the antiferromagnetic spin valve devices.

The spin valve effect was also found in the BLGs being intercalated between ferromagnetic insulator at the top and antiferromagnetic insulator at the bottom, as shown in Fig. 4(d-f). For the BLGs with  $\lambda_{FM,1}^z = \lambda_{AF,2}^z = \lambda_F$  with  $\lambda_F$  being the temporary notation for these systems, the Hubbard interaction slightly enlarges the band

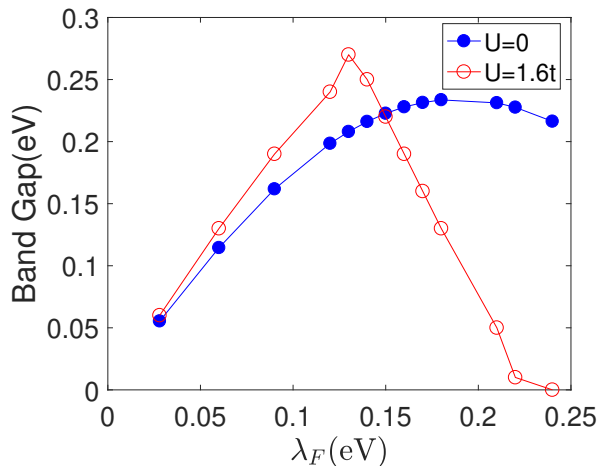


FIG. 5: The bulk band gap versus  $\lambda_{FM,1}^z = \lambda_{AF,2}^z = \lambda_F$  of the BLGs being intercalated between ferromagnetic insulator at the top and antiferromagnetic insulator at the bottom for noninteracting and interacting electron.

gap(Fig. 4(d)). For the BLGs with larger exchange field  $\lambda_F$ , the Hubbard interaction more significantly enlarges the band gap, as shown in Fig. 5. However, with  $\lambda_F$  being larger than 0.13 eV, the trend reverses that the Hubbard interaction significantly suppresses the band gap. When the strength of  $\lambda_F$  reach the threshold at 0.24 eV, the band gap is closed by the Hubbard interaction, implying the insulator to metal phase transition driven by the coexisting of the antiferromagnetic, ferromagnetic exchange field and the electron-electron interaction.

As comparison, the band structure of the BLGs being intercalated between nonmagnetic substrates is plotted in Fig. 4(g), which shows that the Hubbard interaction suppresses the band gap [62]. For the ferromagnetic spin valve consisted of the BLGs being intercalated between two ferromagnetic insulators, the Hubbard interaction does not significantly change the band gap, as shown in Fig. 4(h) and (i). In general, in the presence of the Hubbard interaction, the band gap of the antiferromagnetic spin valve is more sensitive to the changing of the magnetization orientation than that of the ferromagnetic spin valve.

## B. Topological edge states

Because both surface of the BLGs are proximitized to (anti)ferromagnetic insulators, no proximity to TMDCs is feasible. Thus, we neglect the presence of intrinsic SOC. The Rashba SOC could be induced by intercalation of heavy metal atoms between two graphene layers. Firstly, we investigate the BLGs being intercalated being antiferromagnetic insulators with the presence of Rashba SOC, which is modelled by the Hamiltonian  $\sum_{\ell} (H_{0,\ell} + H_{AF,\ell}^z + H_{R,\ell}) + H_{\perp}$ . For the BLGs

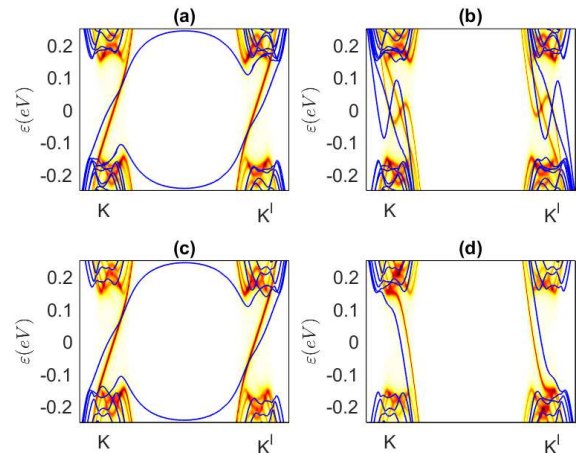


FIG. 6: The band structure and spectral function of the zigzag nanoribbon of the BLGs with domain wall in the middle of the ribbon. The edge states at the open boundaries and the domain wall are separately plotted in the left and right columns, respectively. The left(right) region of the nanoribbon has parameters  $\lambda_{AF,1}^z = -\lambda_{AF,2}^z = 0.28$  eV ( $\lambda_{AF,1}^z = -\lambda_{AF,2}^z = -0.28$  eV) and  $2\lambda_R/3 = 0.3$  eV in (a,b). The left(right) region of the nanoribbon has parameters  $\lambda_{AF,1}^z = -\lambda_{AF,2}^z = 0.28$  eV and  $2\lambda_R/3 = 0.3$  eV ( $\lambda_{AF,1}^z = \lambda_{AF,2}^z = 0.28$  eV and  $\lambda_R = 0$  eV) in (c,d). The total width of the ribbon is 25.56 nm.

with  $\lambda_{AF,1}^z = \lambda_{AF,2}^z$ , additional presence of the Rashba SOC modifies the band gap. The Chern number and valley Chern number remain being zero. For the BLGs with  $\lambda_{AF,1}^z = -\lambda_{AF,2}^z$ , additional presence of nonzero Rashba SOC open the band gap at the intrinsic Fermi level. After the gap is opened, the well defined Chern number is equal to  $2 \cdot \text{sign}(\lambda_{AF,1}^z)$  and the valley Chern number remain being zero. Because of the nonzero Chern number, the quantized charge Hall conductance is  $\sigma_{yx} = Ce^2/h$  [37, 38]. The BLGs is in the quantum anomalous Hall(QAH) phase. The domain wall between two regions with different Chern number host localized edge states. The number of the edge states equates to the difference between the two Chern numbers. This feature is confirmed by the tight binding calculation of the band structures of zigzag nanoribbon with domain wall in the middle. With the CPT method, the spectral function can be spatially integrated on certain region, so that the dispersions of the edge states at the open boundaries and those at the domain wall can be plotted separately. If the domain wall separate two regions with Chern number being 2 and  $-2$ , the band structures of the edge states at the open boundaries and those at the domain wall are plotted in Fig. 6(a) and (b), respectively. For each type of edge states, the dispersions in K and K' valley is the same. One of the edge states at the domain wall has nearly linear dispersion, while the other edge state has oscillating dispersion at the middle of the bulk gap. In the presence of the Hubbard interaction, the band width

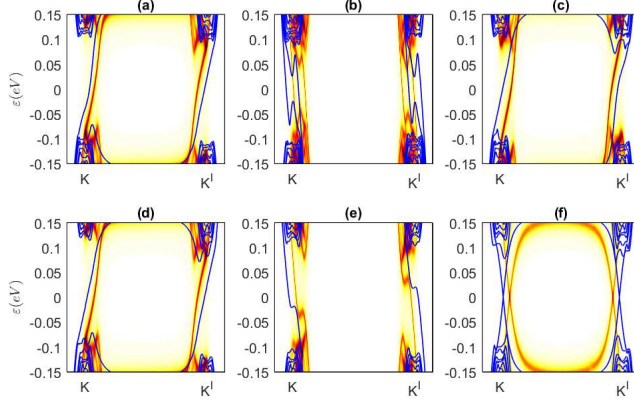


FIG. 7: The same type of plotting as Fig. 6. The edge states at the left open boundary, the domain wall in the middle and the right open boundary of the nanoribbon are separately plotted in the left, middle and right columns, respectively. The left(right) region of the nanoribbon has parameters  $\lambda_{FM,1}^z = -\lambda_{AF,2}^z = 0.17$  eV ( $\lambda_{FM,1}^z = -\lambda_{AF,2}^z = -0.17$  eV) and  $2\lambda_R/3 = 0.082$  eV in (a-c). The left(right) region of the nanoribbon has parameters  $\lambda_{FM,1}^z = -\lambda_{AF,2}^z = 0.17$  eV and  $2\lambda_R/3 = 0.082$  eV ( $\lambda_{FM,1}^z = \lambda_{AF,2}^z = 0.17$  eV and  $\lambda_R = 0$  eV) in (d-f). The total width of the ribbon is 42.6 nm.

of the segment of the edge state band structure with oscillating dispersion is suppressed, as shown by the spectral function in Fig. 6(b). At the domain wall separating two regions with Chern numbers being 2 and 0, only the edge state with nearly linear dispersion appears, as shown in Fig. 6(d). Because the K and K' valley dispersions of the edge states at the domain wall are the same, these edge state support one-way charge conductivity at Fermi level. For realistic materials, the parameters are smaller than those in Fig. 6, so that the finite size effect couple the edge states at the open boundaries and that at the domain wall. But the finite size effect become insignificant for nanoribbon with larger width.

The BLGs being intercalated between antiferromagnetic insulator and ferromagnetic insulator with the presence of Rashba SOC, which is modelled by the Hamiltonian  $\sum_{\iota} (H_{0,\iota} + H_{R,\iota}) + H_{AF,1}^z + H_{FM,2}^z + H_{\perp}$  or  $\sum_{\iota} (H_{0,\iota} + H_{R,\iota}) + H_{FM,1}^z + H_{AF,2}^z + H_{\perp}$  have similar topological properties. The BLGs with  $\lambda_{AF,1}^z = \lambda_{FM,2}^z$  or  $\lambda_{FM,1}^z = -\lambda_{AF,2}^z$  have nonzero Chern number being  $\mathcal{C} = 2 \cdot \text{sign}(\lambda_{FM,2}^z)$  or  $\mathcal{C} = 2 \cdot \text{sign}(\lambda_{FM,1}^z)$ , respectively, assuming  $\lambda_R \neq 0$ . On the other hand, the BLGs with  $\lambda_{AF,1}^z = -\lambda_{FM,2}^z$  or  $\lambda_{FM,1}^z = \lambda_{AF,2}^z$  have zero Chern number. The valley Chern number of these BLGs are zero. For the domain wall that separates two regions with Chern number being +2 and -2, the band structure and spectral function are plotted in Fig. 7(a-c). The dispersions of the localized edge states are nearly linear at the intrinsic Fermi level, which are the same at K and K' valleys. The presence of the Hubbard interaction enlarge the bandwidth with nearly linear dispersion around the

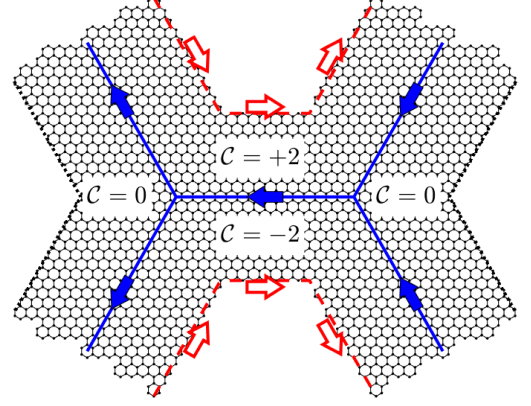


FIG. 8: The scheme of three-way current partition and recombination at the junction of three domain walls.

intrinsic Fermi level. In order to optimally construct the domain wall that with Chern number being  $\pm 2$  and 0, engineer of the strength of the exchange field and Rashba SOC is required, because the Hubbard interaction and the Rashba SOC could either enlarge or suppress the bulk band gap. The optimal parameters were found to be  $\lambda_{FM,1}^z = -\lambda_{AF,2}^z = 0.17$  eV and  $2\lambda_R/3 = 0.082$  eV for one region with  $\mathcal{C} = 2$  and  $\lambda_{FM,1}^z = \lambda_{AF,2}^z = 0.17$  eV and  $2\lambda_R/3 = 0$  eV for the other region with  $\mathcal{C} = 0$ . The band structure and spectral function of this nanoribbon are plotted in Fig. 7(d-f). The edge states at the open boundary of the  $\mathcal{C} = 0$  side have regular feature with both positive and negative dispersion in both valleys (Fig. 7(f)). Two of the four edge states at the domain wall in Fig. 7(b) are inherited to the domain wall in Fig. 7(e).

Because the Chern number could be one of the three number,  $\pm 2$  or 0, the junction among three regions with three different Chern numbers can be constructed, as shown in Fig. 8. The Chern number of each regions are labeled in the figure. The junction of three domain walls support current partition or recombination [66, 67]. In Fig. 8, the topological domain walls are marked by solid(blue) lines, with solid(blue) arrow indicating the direction of the one-way charge current at Fermi level. The three-way junction at the left support current partition, and that at the right support current recombination. The open boundaries of the regions with  $\mathcal{C} = \pm 2$  are marked by red(dashed) lines, which also support one-way charge current labeled by the empty red arrows. The open boundaries of the region with  $\mathcal{C} = 0$  is marked by black(dotted) lines. On the other hand, the junction among four regions with Chern number being +2, -2, +2 and -2 along (counter)clockwise sequence support current partition and recombination as well [39]. The large scale complicated integrated spintronic circuits could be constructed by jigsaw of regions with varying Chern numbers.

### C. Phase diagram in the coexistence of Hubbard interaction and Rashba SOC

In the absence of the Hubbard interaction, the BLGs with  $\lambda_{AF,1}^z = -\lambda_{FM,2}^z = \lambda_F$  or  $\lambda_{FM,1}^z = \lambda_{AF,2}^z = \lambda_F$  and finite  $\lambda_R$  is topologically trivial. With  $\lambda_R$  being small, the global band gap with zero Chern number exist. With  $\lambda_R$  being sufficiently large, the Chern number is nonzero, but the global gap is closed because the local band gaps of the two valleys do not align. Thus, the BLGs in these phase regimes is not in the QAH phase, but in the Chern topological metallic(CTM) phase. The local band gap of each valley is small, so that the topological edge states at the open boundary in each valley [68] are weakly localized. The additional presence of the Hubbard interaction drives the system into the QAH phase with global gap and nonzero Chern number in part of the phase regime. The Chern number is calculated by integrating the Berry curvature of the topological Hamiltonian [69–74], which is the inverse of the zero frequency Green's function given by the CPT method. The numerical result of the phase diagram is plotted in Fig. 9(a). Three regimes with Chern number being 2,  $-2$  and  $-4$  are identified. In the regimes with  $\mathcal{C} = -2$  or  $\mathcal{C} = -4$ , the gaps of the two valleys does not align and then the BLGs are in the CTM phase. In the regimes with  $\mathcal{C} = -2$ , the local band gap of each valley is significantly larger than that of the corresponding non-interacting systems, so that the topological edge states at the open boundary in each valley are more localized. In the regime with  $\mathcal{C} = 2$ , the global gap exists. At the phase boundary between the regimes with  $\mathcal{C} = 2$  and  $\mathcal{C} = 0$  in the phase diagram, the global gap as well as the gap of each valley close at the intrinsic Fermi level. The gap closing is driven exclusively by the Hubbard interaction, because in the corresponding non-interacting model neither the global band gap nor the band gap of each valley closes in this phase regime.

In order to confirm the topological gap of the QAH phase, the band structure of the zigzag nanoribbon of the BLG with  $\lambda_{FM,1}^z = \lambda_{AF,2}^z = 0.4$  eV,  $\lambda_R = 0.2$  eV and  $U = 0$  is plotted in Fig. 9(b), and the spectral functions of the two open boundaries of the same nanoribbon with  $U = 1.6t$  and  $\mathcal{C} = 2$  are plotted in Fig. 9(c) and (d). The band structure of the non-interacting system exhibit feature of the valley polarized metal with the conduction(valence) band of the K(K') valley being partially filled(empty). By contrast, the spectral functions of the interacting system exhibit edge states in the global bulk gap. The left open boundary host two edge states with positive dispersion; the right open boundary host two edge states with positive dispersion, and two other edge states with negative dispersion. The number of the edge states with positive dispersion minus the number of the edge states with negative dispersion equates to the Chern number. For the BLG with  $\lambda_{FM,1}^z = \lambda_{AF,2}^z = 0.1$  eV,  $\lambda_R = 0.2$  eV and  $U = 1.6t$ , thus with  $\mathcal{C} = -2$ , the spectral functions of the two open boundaries are plotted in Fig. 9(e) and (f). The bulk band gaps at K and

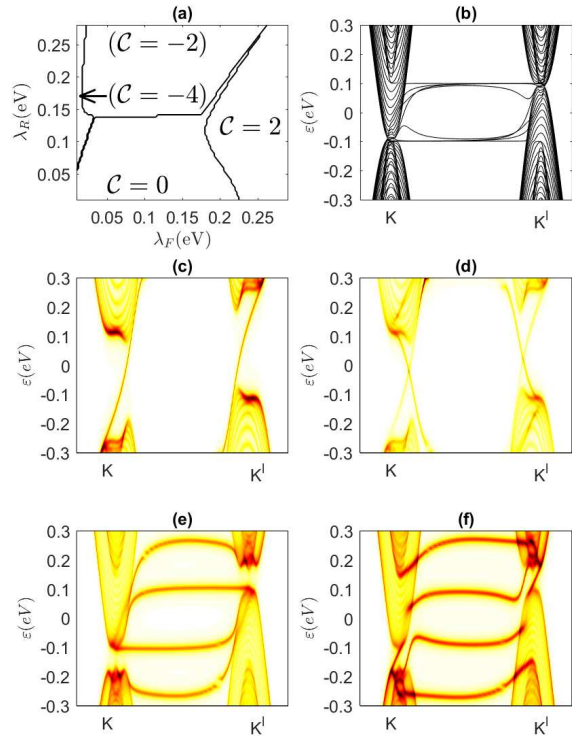


FIG. 9: (a) The phase diagram of the Chern number in the  $(\lambda_F, \lambda_R)$  phase space of the BLGs with  $\lambda_{FM,1}^z = \lambda_{AF,2}^z = \lambda_F$  and  $U = 1.6t$ . The band structure of the zigzag nanoribbon of the BLG with  $\lambda_{FM,1}^z = \lambda_{AF,2}^z = 0.4$  eV,  $\lambda_R = 0.2$  eV and  $U = 0$  in (b). For the same nanoribbon with  $U = 1.6t$  and  $\mathcal{C} = 2$ , the spectral functions of the left and right zigzag open boundaries are plotted in (c) and (d), respectively. The total width of the ribbon is 21.3 nm. For another nanoribbon with  $\lambda_{FM,1}^z = \lambda_{AF,2}^z = 0.1$  eV,  $\lambda_R = 0.2$  eV,  $U = 1.6t$  and  $\mathcal{C} = -2$ , the spectral functions of the left and right zigzag open boundaries are plotted in (e) and (f), respectively. The total width of the ribbon is 42.6 nm.

K' valley do not align. Within the band gap of each valley, two edge states being localized at the right open boundary appear. One of the edge states (the one with smaller (larger) wave number in the K (K') valley) is topologically protected, while the other edge state accidentally crosses the band gap. Although the global band gap does not exist in this BLG system, the novel transportation feature of the topologically protected edge states could be harnessed by tuning the Fermi level into the band gap of one valley.

## IV. CONCLUSION

The spin valves consisted of heterostructures of graphene and (anti)ferromagnetic insulator are studied by solving the tight binding model with the presence of

staggered sublattice exchange field, Hubbard model and the SOC. The band structure of bulk graphenes and domain walls are controlled by the magnetization orientation of the antiferromagnetic substrate(s). Both of the bulk states and localized edge states at the domain walls could be used to construct spin valves devices, whose conductivities of charge, valley or spin currents are controlled by the magnetization orientation. The presence of the Hubbard interaction widens the band gap of the SLGs and BLGs heterostructures with only antiferromagnetic substrate(s). The Hubbard interaction improves the quality of the spin-dependent chiral edge states at the domain wall of the SLGs heterostructures by weakening the finite size effect and widening the effective bandwidth with linear dispersion. For the BLGs heterostructures with mixed substrates of antiferromagnetic and ferromagnetic, the band gap is widened, narrowed or closed by the presence of the Hubbard interaction, if the strength of the exchange field is small, median or large, respectively.

In the additional presence of the SOC in the SLGs with antiferromagnetic substrate, the band structures near to the K and K' point become spin and(or) valley dependent, resulting in spin, valley or spin-valley polarized conductivity at the Fermi level, depending on the strength of Rashba and intrinsic SOC. For the BLGs being driven into metal or insulator by the (anti)ferromagnetic substrates, the additional presence of the Rashba SOC opens the topological band gap with Chern number being  $\pm 2$ , or modifies the band gap without changing the Chern number, respectively. At the domain wall between regions with different Chern number, the localized edge

states are studied by solving the tight binding model of the zigzag nanoribbon with sufficient width. The dispersions of the localized edge states at K and K' valleys are the same, implying one-way charge conductivity at Fermi level. The additional presence of the Hubbard interaction improves the quality of the localized edge states by widening the bandwidth with nearly linear one-way dispersion. The three-way current partition or recombination devices consisted of the junction of three regions with three different Chern numbers are proposed, which could be the building block for large scale integrated antiferromagnetic spintronic systems. For the BLGs that is not driven into the QAH phase by the co-presence of the (anti)ferromagnetic substrates and the Rashba SOC, the additional presence of the Hubbard interaction could drive the systems into the QAH phase. Further studies of the antiferromagnetic spin valve systems would require the search or engineering of realistic antiferromagnetic materials with surface lattice being matched to graphene, as well as appropriate adatom doping that induce SOC simultaneously.

### Acknowledgments

The project is supported by the National Natural Science Foundation of China (Grant: 11704419).

### References

- 
- [1] M. N. Baibich, J. M. Broto, A. Fert, F. Nguyen Van Dau, F. Petroff, P. Etienne, G. Creuzet, A. Friederich, and J. Chazelas, *Phys. Rev. Lett.* **61**, 2472 (1988).
  - [2] G. Binasch, P. Gruber, F. Saurenbach, and W. Zinn, *Phys. Rev. B* **39**, 4828 (1989).
  - [3] M. Julliere, *Phys. Lett. A* **54**, 225 (1975).
  - [4] J. S. Moodera, L. R. Kinder, T. M. Wong, and R. Meserve, *Phys. Rev. Lett.* **74**, 3273 (1995).
  - [5] B. Dieny, V. S. Speriosu, S. Metin, S. S. Parkin, B. A. Gurney, P. Baumgart, and D. R. Wilhoit, *J. Appl. Phys.* **69**, 4774 (1991).
  - [6] Dmytro Pesin and Allan H. MacDonald, *Nature Materials*, **11**, 409C416(2012).
  - [7] Wei Han, Roland K. Kawakami, Martin Gmitra and Jaroslav Fabian, *Nature Nanotechnology*, **9**, 794C807(2014).
  - [8] Narjes Kheirabadi, Azizollah Shafiekhani and Morteza Fathipour, *Superlattices and Microstructures*, **74**, 123(2014).
  - [9] Phaeton Avouris, Zhihong Chen and Vasili Perebeinos, *Nature Nanotechnology*, **2**, 605C615(2007).
  - [10] A. H. Castro Neto, F. Guinea, N. M. R. Peres, K. S. Novoselov, and A. K. Geim, *Rev. Mod. Phys.* **81**, 109(2009).
  - [11] H. Min, J. E. Hill, N. A. Sinitsyn, B. R. Sahu, L. Kleinman, and A. H. MacDonald, *Phys. Rev. B* **74**, 165310 (2006).
  - [12] D. Huertas-Hernando, F. Guinea, and A. Brataas, *Phys. Rev. B* **74**, 155426 (2006).
  - [13] J. C. Boettger and S. B. Trickey, *Phys. Rev. B* **75**, 121402(R) (2007).
  - [14] Jose H. Garcia, Marc Vila, Aron W. Cummings and Stephan Roche, *Chem. Soc. Rev.*, **47**, 3359(2018).
  - [15] Marko M. Grujic, Milan Z. Tadic, and Francois M. Peeters, *Phys. Rev. Lett.* **113**, 046601(2014).
  - [16] Da-Ping Liu, Zhi-Ming Yu, and Yu-Liang Liu, *Phys. Rev. B* **94**, 155112(2016).
  - [17] M. Inglot, V. K. Dugaev, E. Ya. Sherman, and J. Barnas, *Phys. Rev. B* **89**, 155411 (2014).
  - [18] J. Rioux and G. Burkard, *Phys. Rev. B* **90**, 035210 (2014).
  - [19] M. Inglot, V. K. Dugaev, E. Ya. Sherman, and J. Barnas, *Phys. Rev. B* **91**, 195428 (2015).
  - [20] V. Kaladzhyan, P. P. Aseev, and S. N. Artemenko, *Phys. Rev. B* **92**, 155424 (2015).
  - [21] Ma Luo and Zhibing Li, *Phys. Rev. B* **96**, 165424(2017).
  - [22] Reinaldo Zapata-Pena, Bernardo S. Mendoza, and Anatoli I. Shkrebtii, *Phys. Rev. B* **96**, 195415(2017).
  - [23] J. B. S. Mendes, O. Alves Santos, L. M. Meireles, R. G. Lacerda, L. H. Vilela-Leao, F. L. A. Machado, R. L.

- Rodriguez-Suarez, A. Azevedo, and S. M. Rezende, *Phys. Rev. Lett.* 115, 226601(2015).
- [24] M. Gurram, S. Omar, S. Zihlmann, P. Makk, C. Schonenberger, and B. J. van Wees, *Phys. Rev. B* 93, 115441(2016).
- [25] S. Omar and B. J. van Wees, *Phys. Rev. B* 95, 081404(R)(2017).
- [26] Emmanuel I. Rashba, *Phys. Rev. B*, 79, 161409(R)(2009).
- [27] Zhenhua Qiao, Shengyuan A. Yang, Wanxiang Feng, Wang-Kong Tse, Jun Ding, Yugui Yao, Jian Wang and Qian Niu, *Phys. Rev. B*, 82, 161414(R)(2010).
- [28] Jayakumar Balakrishnan, Gavin Kok Wai Koon, Ahmet Avsar, Yuda Ho, Jong Hak Lee, Manu Jaiswal, Seung-Jae Baeck, Jong-Hyun Ahn, Aires Ferreira, Miguel A. Cazalilla, Antonio H. Castro Neto and Barbaros Ozyilmaz, *Nature Communications*, 5, 4748(2014).
- [29] Fufang Xu, Baolei Li, Hui Pan and Jia-Lin Zhu, *Phys. Rev. B*, 75, 085431(2007).
- [30] M. Gmitra and J. Fabian, *Phys. Rev. B* 92, 155403(2015).
- [31] M. Gmitra, D. Kochan, P. Hogg, and J. Fabian, *Phys. Rev. B* 93, 155104(2016).
- [32] Z. Wang, D.-K. Ki, H. Chen, H. Berger, A. H. MacDonald, and A. F. Morpurgo, *Nat. Commun.* 6, 8339(2015).
- [33] Manuel Offidani, Mirco Milletter, Roberto Raimondi, and Aires Ferreira, *Phys. Rev. Lett.* 119, 196801(2017).
- [34] Tobias Frank, Petra Hogg, Martin Gmitra, Denis Kochan, and Jaroslav Fabian, *Phys. Rev. Lett.* 120, 156402(2018).
- [35] Abdulrhman M. Alsharari, Mahmoud M. Asmar, and Sergio E. Ulloa, *Phys. Rev. B* 97, 241104(R)(2018).
- [36] Vo Tien Phong, Niels R Walet and Francisco Guinea, *2D Mater.*, 5, 014004(2018).
- [37] Zhenhua Qiao, Shengyuan A. Yang, Wanxiang Feng, Wang-Kong Tse, Jun Ding, Yugui Yao, Jian Wang, and Qian Niu, *Phys. Rev. B* 82, 161414(R)(2010).
- [38] Motohiko Ezawa, *Phys. Rev. Lett.* 109, 055502(2012).
- [39] Yafei Ren, Junjie Zeng, Ke Wang, Fuming Xu, and Zhenhua Qiao, *Phys. Rev. B* 96, 155445(2017).
- [40] Yuan Liu, Nathan O. Weiss, Xidong Duan, Hung-Chieh Cheng, Yu Huang and Xiangfeng Duan, *Nature Reviews Materials*, 1, 16042(2016).
- [41] C. Cardoso, D. Soriano, N. A. Garcia-Martinez, and J. Fernandez-Rossier, *Phys. Rev. Lett.* 121, 067701(2018).
- [42] T. Jungwirth, X. Marti, P. Wadley and J. Wunderlich, *Nature Nanotechnology*, 11, 231C241(2016).
- [43] V. Baltz, A. Manchon, M. Tsoi, T. Moriyama, T. Ono, and Y. Tserkovnyak, *Rev. Mod. Phys.* 90, 015005(2018).
- [44] Xi He, Yi Wang, Ning Wu, Anthony N. Caruso, Elio Vescovo, Kirill D. Belashchenko, Peter A. Dowben and Christian Binek, *Nature Materials*, 9, 579C585(2010).
- [45] Satya Prakash Pati, Muftah Al-Mahdawi, Shujun Ye, Yohei Shiokawa, Tomohiro Nozaki, and Masashi Sahashi, *Phys. Rev. B* 94, 224417(2016).
- [46] Tobias Kampfrath, Alexander Sell, Gregor Klatt, Alexej Pashkin, Sebastian Mahrlein, Thomas Dekorsy, Martin Wolf, Manfred Fiebig, Alfred Leitenstorfer and Rupert Huber, *Nature Photonics*, 5, 31C34(2011).
- [47] Stephen M. Wu, Wei Zhang, Amit KC, Pavel Borisov, John E. Pearson, J. Samuel Jiang, David Lederman, Axel Hoffmann, and Anand Bhattacharya, *Phys. Rev. Lett.* 116, 097204(2016).
- [48] S. Raghu, Xiao-Liang Qi, C. Honerkamp, and Shou-Cheng Zhang, *Phys. Rev. Lett.* 100, 156401(2008).
- [49] Mengsu Chen, Hoi-Yin Hui, Sumanta Tewari, and V. W. Scarola, *Phys. Rev. B* 97, 035114(2018).
- [50] Ali Hallal, Fatima Ibrahim, Hongxin Yang, Stephan Roche and Mairbek Chshiev, *2D Mater.* 4 025074(2017).
- [51] Stephane Pairault, David Senechal, and A.-M. S. Tremblay, *Phys. Rev. Lett.* 80, 5389(1998).
- [52] D. Senechal, D. Perez, and M. Pioro-Ladriere, *Phys. Rev. Lett.* 84, 522(2000).
- [53] David Senechal, Danny Perez, and Dany Plouffe, *Phys. Rev. B* 66, 075129(2002).
- [54] F Grandi, F Manghi, O Corradini, C M Bertoni and A Bonini, *New J. Phys.* 17, 023004(2015).
- [55] F. Grandi, F. Manghi, O. Corradini, and C. M. Bertoni, *Phys. Rev. B* 91, 115112(2015).
- [56] Ma Luo and Zhibing Li, arXiv:1804.07868(2018).
- [57] Fan Zhang, Allan H. MacDonald and Eugene J. Mele, *Proc Natl Acad Sci U S A.*,110(26), 10546 10551(2013).
- [58] Zhenhua Qiao, Xiao Li, Wang-Kong Tse, Hua Jiang, Yugui Yao, and Qian Niu, *Phys. Rev. B* 87, 125405(2013).
- [59] G. W. Semenoff, V. Semenoff, and Fei Zhou, *Phys. Rev. Lett.* 101, 087204(2008).
- [60] M. Zarenia, O. Leenaerts, B. Partoens, and F. M. Peeters, *Phys. Rev. B* 86, 085451(2012).
- [61] Kyu Won Lee and Cheol Eui Lee, *Phys. Rev. B* 95, 195132(2017).
- [62] Jin-Rong Xu, Ze-Yi Song, Hai-Qing Lin, and Yu-Zhong Zhang, *Phys. Rev. B* 93, 035109(2016).
- [63] Jin-Rong Xu, Ze-Yi Song, Chen-Guang Yuan, and Yu-Zhong Zhang, *Phys. Rev. B* 94, 195103(2016).
- [64] Di Xiao, Gui-Bin Liu, Wanxiang Feng, Xiaodong Xu, and Wang Yao, *Phys. Rev. Lett.* 108, 196802(2012).
- [65] C. L. Kane and E. J. Mele, *Phys. Rev. Lett.* 95, 226801(2005).
- [66] Ma Luo, arXiv:1805.09995(2018).
- [67] Ma Luo, arXiv:1804.09881(2018).
- [68] Hui Pan, Xin Li, Zhenhua Qiao, Cheng-Cheng Liu, Yugui Yao and Shengyuan A Yang, *New J. Phys.*, 16, 123015(2014).
- [69] Zhong Wang, Xiao-Liang Qi, and Shou-Cheng Zhang, *Phys. Rev. Lett.* 105, 256803(2010).
- [70] V. Gurarie, *Phys. Rev. B* 83, 085426(2011).
- [71] Zhong Wang and Shou-Cheng Zhang, *Phys. Rev. X* 2, 031008(2012).
- [72] Zhong Wang, Xiao-Liang Qi, and Shou-Cheng Zhang, *Phys. Rev. B* 85, 165126(2012).
- [73] Zhong Wang and Binghai Yan, *J. Phys.: Condens. Matter* 25, 155601(2013).
- [74] Yuan-Yao He, Han-Qing Wu, Zi Yang Meng, and Zhong-Yi Lu, *Phys. Rev. B* 93, 195163(2016).